Atomic Layer Deposition Stabilizes Nanocrystals, Enabling Reliably High-Performance Quantum Dot LEDs

Haoyue Wan, Pan Xia, Euidae Jung, Muhammad Imran, Ruiqi Zhang, Yiqing Chen, Julian A. Steele, Sabah Gaznaghi, Yanjiang Liu, Ya-Kun Wang, Lianzhou Wang, Yu-Ho Won, Kwang-Hee Kim, Vladimir Bulović,* Sjoerd Hoogland, and Edward H. Sargent*

Quantum dot light-emitting diodes (QD-LEDs) with stable high efficiencies are crucial for next-generation displays. However, uncontrollable aging, where efficiency initially increases during storage (positive aging) but is entirely lost upon extended aging (negative aging), hinders further device development. It is uncovered that it is chemical changes to nanocrystal (NC)-based electron transport layer (ETL) that give rise to positive aging, their drift in structure and morphology leading to transiently improved charge injection balance. Using grazing-incidence small-angle X-ray scattering, it is found that ZnMgO NCs undergo size-focusing ripening during aging, improving size uniformity and creating a smoother energy landscape. Electron-only device measurements reveal a sevenfold reduction in trap states, indicating enhanced surface passivation of ZnMgO. These insights, combined with density functional theory calculations of ZnMgO surface binding, inspire an atomic layer deposition (ALD) strategy with Al_2O_3 to permanently suppress surface traps and inhibit NC growth, effectively eliminating aging-induced efficiency loss. This ALD-engineered ZnMgO ETL enables reproducible external quantum efficiencies (EQEs) of 17% across 30 batches of LEDs with a T_{60} of 60 h at an initial luminance of 4500 cd m^{-2}, representing a 1.6-fold increase in EQE and a tenfold improvement in operating stability compared to control devices.

1. Introduction

Colloidal quantum dot (QD)-based light-emitting diodes (LEDs) are emerging in display technology due to their luminescence efficiency, narrow emission linewidth, and wide range of tunable wavelengths.[1–4] A conventional thin-film LED structure, processed through the solution, consists of a pair of electrodes sandwiching an electron transport layer (ETL), a hole transport layer (HTL), and a light-emitting active layer.[2] In this configuration, charge carriers are injected from the electrodes through the transport layers, and radiatively recombine in the active layer. ZnO-based nanocrystals (NCs) are particularly favored as ETL materials due to their excellent optoelectronic compatibility with the emissive active layer.[5–10]

An uncontrollable aging phenomenon poses a challenge to the widespread adoption of QD-LEDs with ZnMgO-based ETLs. Unlike typical optoelectronic

H. Wan, P. Xia, E. Jung, M. Imran, Y. Chen, Y. Liu, Y.-K. Wang,
S. Hoogland, E. H. Sargent
Department of Electrical and Computer Engineering
University of Toronto
10 King's College Road, Toronto, Ontario M5S 3G4, Canada
E-mail: ted.sargent@utoronto.ca
R. Zhang, V. Bulović
Department of Electrical Engineering and Computer Science
Massachusetts Institute of Technology
Cambridge, MA 02139, USA
E-mail: bulovic@mit.edu

The ORCID identification number(s) for the author(s) of this article can be found under https://doi.org/10.1002/adma.202418300

J. A. Steele, S. Gaznaghi, L. Wang
Australian Institute for Bioengineering and Nanotechnology
The University of Queensland
Brisbane, QLD 4072, Australia
J. A. Steele
School of Mathematics and Physics
The University of Queensland
Brisbane, QLD 4072, Australia
L. Wang
Nanomaterials Centre
School of Chemical Engineering
The University of Queensland
Brisbane, QLD 4072, Australia
Y.-H. Won, K.-H. Kim
Samsung Advanced Institute of Technology
Samsung Electronics
Suwon, Republic of Korea

**ADVANCED
SCIENCE NEWS**

www.advancedsciencenews.com
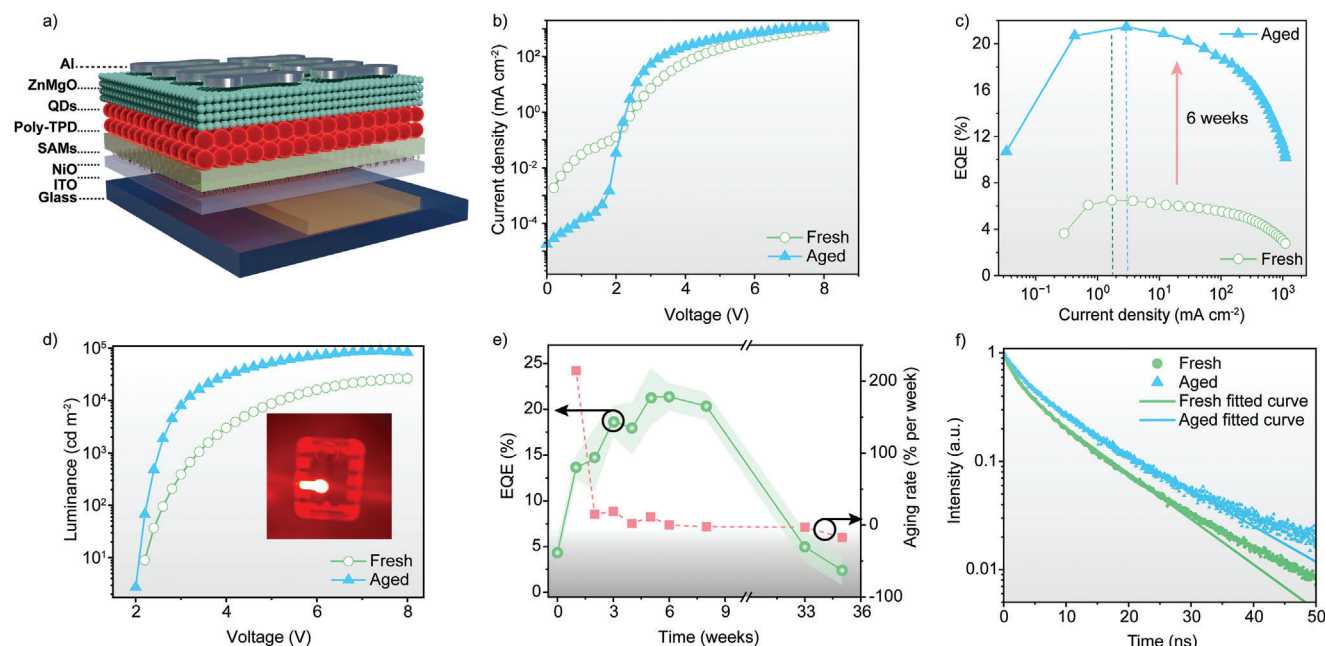
**ADVANCED
MATERIALS**

www.advmat.de

Figure 1. Significant Changes in QD-LED Efficiency Due to Aging. a) Device structure of the fabricated InP QD-LEDs. b) Current density-voltage charac-teristics, c) EQE-current density characteristics, d) luminance-voltage characteristics of devices measured immediately after fabrication (fresh) and after 6 weeks of aging under nitrogen (aged). The inset in panel (d) shows the red emission of the QD-LED. e) EQE and aging rate of devices over 36 weeks of storage, with the shaded area representing the error bars. f) Time-resolved photoluminescence decay curves of the QD-LED were measured both as fresh and after 6 weeks of aging.

devices that degrade over time, QD-LEDs with ZnO ETL exhibit unexpected positive aging, where efficiency initially improves over weeks before degrading.[11–15] While positive aging enhances efficiency, its unpredictability leads to inconsistent device perfor-mance. This lack of consistency presents a significant barrier to the practical application of QD-LED technology, as reliable and predictable performance is crucial for productization.[3,6]

Pinpointing the cause of this positive aging remains difficult, with some reports attributing improvements to outgassing from UV-curable encapsulants,[11,12] but variations in aging conditions make this difficult to establish as a main or universal culprit.

We studied the mechanism of positive aging in red InP QD-LEDs without encapsulation. Our findings demonstrate that pos-itive aging is an intrinsic property of the devices, not depen-dent on the encapsulation process. Through device characteri-zation, we identified the size-focusing ripening of ZnMgO NCs as the primary contributor. This process reduces surface traps and improves homogeneity within the ZnMgO layer, leading to enhanced conductivity, but requires a long aging period and un-certain results. To overcome this limitation and achieve optimal performance from freshly fabricated devices, we developed a new fabrication strategy. By incorporating an atomic layer deposition (ALD) aluminum oxide (Al_2O_3) onto ZnMgO, we effectively pas-sivated the surface and completely suppressed the size-focusing ripening of the ZnMgO layer. This strategy enables freshly fab-ricated QD-LEDs to achieve reproducibly high external quantum efficiencies (EQEs) of 17% without the need for a slow aging pro-cess. Additionally, the devices exhibit a significant improvement in stability, with a T_{60} of 60 h at an initial luminance of 4500 cd

m^{-2} which is a tenfold improvement in T_{60} compared to unen-capsulated devices without the ALD layer. This method passivates NC films, enhancing stability in both electronic devices and elec-trocatalysis processes.

2. Results and Discussion

Red InP-based QD-LEDs were fabricated using previously published structures to assess the degree of positive aging. The state-of-the-art structure includes indium tin oxide (ITO/NiOx/4-trifluoromethyl benzoic acid (4-CF$_3$-BA)/poly(4-butyl-N, N-diphenylaniline) (poly-TPD)/InP QD/ZnMgO NCs/Al) (**Figure 1a**).[8,15,16] The devices undergo shelf aging in a nitrogen-filled glovebox for over thirty-five weeks. We measure the current density-voltage (J-V) characteristics of both fresh and aged devices. The peak EQE is reached after six weeks of storage, accompanied by a significant reduction in dark current and an increase in current density at high voltages (Figure 1b). Quan-titative analysis of the EQE-luminance and luminance-voltage data reveals a 230% and 235% increase in EQE and luminance, respectively, after six weeks of aging (Figure 1c,d).

To understand the long-term aging behavior, we monitored the devices over the course of 36 weeks (Figure 1e). We observed a dramatic increase in EQE in the first six weeks of aging, followed by a decrease. Eventually, after thirty weeks of aging, the EQE fell below the performance of fresh devices. This decline is poten-tially due to oxygen migration from ZnMgO to the active layer,[17] ETL degradation,[18] and/or oxidation of InP QDs.[19]

The rate of increase in performance we observe is much larger than those reported in the literature,[11,12,14] which prompted us
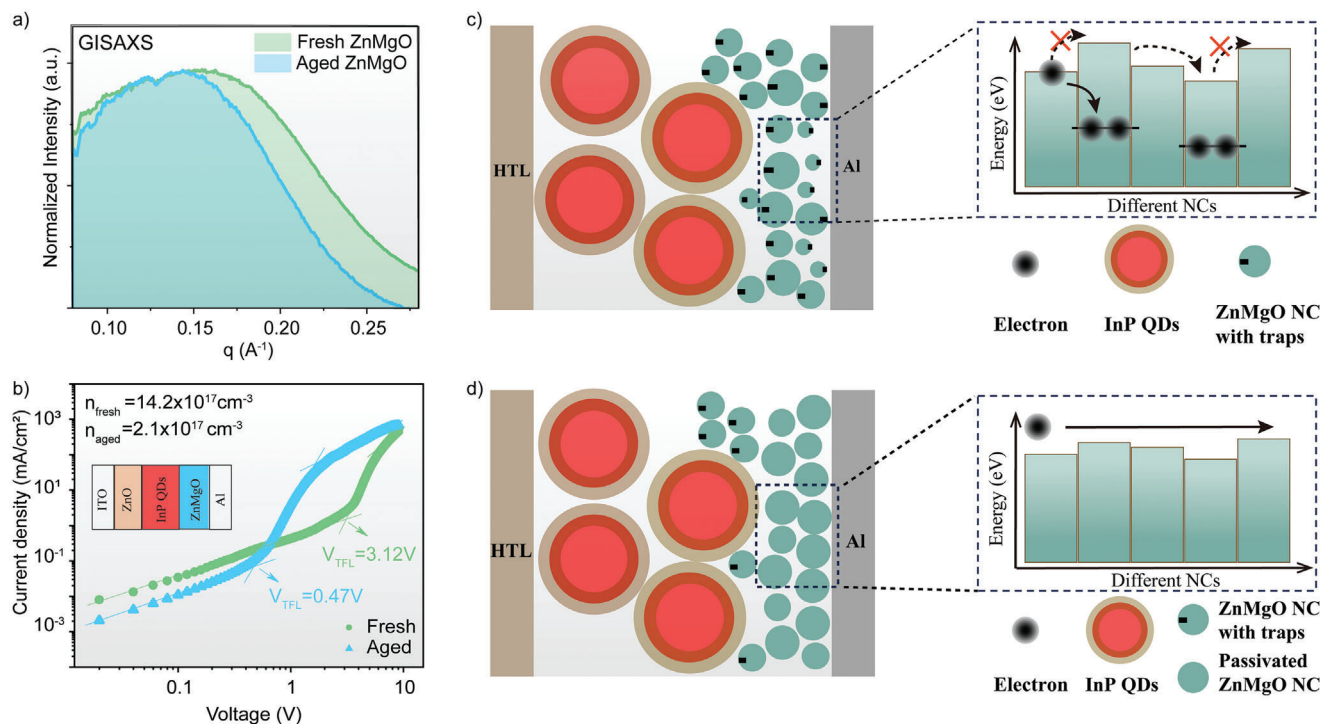
**ADVANCED
SCIENCE NEWS**

www.advancedsciencenews.com

**ADVANCED
MATERIALS**

www.advmat.de

Figure 2. Mechanism of Aging in ZnMgO NCs. a) Azimuthally integrated intensities of the GISAXS diffraction peak for fresh and aged ZnMgO samples. They show the distribution of interdot d spacing ($d = 2\pi\ q^{-1}$) in the NC assembly. The aged films (blue) exhibit a ≈13% increase in d spacing and narrower peaks by ≈20% compared to fresh films (green). b) Current density-voltage characteristics of electron-only fresh and aged devices. c) In fresh devices, ZnMgO NCs exhibit size heterogeneity and numerous traps, leading to low conductivity. d) During aging, the ZnMgO film undergoes a size-focusing ripening process, resulting in a more uniform NC size distribution and reduced surface traps. This improved uniformity and reduced amount of trapping sites enhance conductivity due to a more homogenous energy landscape for electrons and minimized electron trapping.

to investigate the origin of the positive aging effect in our devices. According to the definition of EQE (see supplementary information note 1), EQE is proportional to both photoluminescence quantum yield (PLQY) and balanced carrier injection. The PLQY of the InP QD devices increases by 18% following aging (from 61% to 79%), whereas InP QD films exhibit a stable PLQY of ≈86% over two weeks (Figure S1, Supporting Information). Strikingly, whereas the PLQY improvement is 1.3x, the EQE increase is 3.3x. Therefore, we attribute this substantial enhancement primarily to improved balanced carrier injection (η_r, the fraction of injected charges that form excitons in the QDs) upon aging. This improved efficiency indicates a more balanced injection of electrons and holes. This conclusion is further supported by the increased current density observed at voltages above turn-on in the J-V curves after aging (see Figure 1b).

To identify the carrier injection layer limiting the current density in unaged LEDs, we fabricated a batch of devices with varying ETL and HTL thicknesses. The current density decreases significantly as the thickness of the ETL increases (Figure S2a, Supporting Information), while it remains unaffected by changing the HTL thickness. This suggests that the injection of electrons, rather than holes, limits the current density in fresh devices (Figure S2b, Supporting Information).[20,21]

Next, we fabricated devices with a similar structure but without the InP QD layer (ITO/NiOx/poly-TPD/ZnMgO/Al) to examine the electroluminescence (EL) from ZnMgO or poly-TPD. We observed the EL ratio of poly-TPD to ZnMgO increases with in-

creasing voltage (Figure S2c, Supporting Information). This observation can be explained by the recombination center shifting to the poly-TPD layer as voltage increases, indicating that the fresh ZnMgO-based ETL devices have lower conductivity than the HTL (Figure S2d, Supporting Information). This disparity in conductivity leads to an imbalanced injection of holes and electrons, which we identify as a primary cause of the low EQE observed in our fresh devices.

We hypothesize that the conductivity of our ZnMgO layer increases after aging, leading to improved carrier balance and a higher EQE in aged devices. The conductivity change may arise from changes in the size distribution of NCs,[22] reduced interfacial traps,[23] and improved passivation.[24] To investigate the changes in the aged ZnMgO layer, we performed grazing-incidence small-angle scattering (GISAXS) experiments on fresh and aged ZnMgO. We focus on the peak between 0.1–0.2 $Å^{-1}$, corresponding to an average dot-to-dot distance of 3.1 to 6.3 nm (**Figure 2a**). Assuming NCs maintain the same packing, GISAXS results reveal that aged ZnMgO film exhibited a ≈20% narrower dot-to-dot distance and a slight increase in the average dot size from 4.0 to 4.5 nm. (see Note S2, Supporting Information) This increased uniformity in dot size leads to a more orderly arrangement of energy levels, thereby enhancing electron conductivity[22,25] (Figure 2c,d).

To elucidate the trap density within ZnMgO NCs, electron-only devices with the following structure: ITO/ZnO/InP QD/ZnMgO/Al were fabricated. We measured the current-
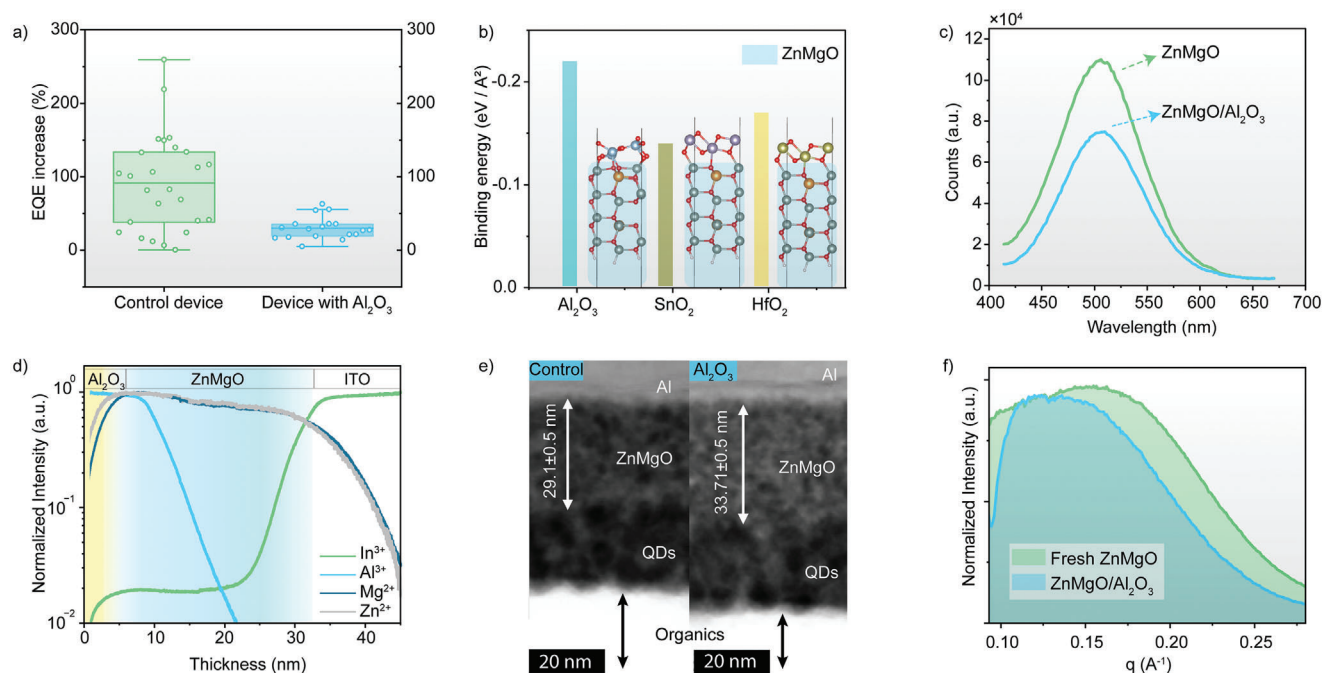
**ADVANCED
SCIENCE NEWS**

www.advancedsciencenews.com

**ADVANCED
MATERIALS**

www.advmat.de

Figure 3. Al_2O_3 Passivation of ZnMgO Layer. a) Increased EQE upon aging (boxplots, ≈30 for each device) for Al_2O_3-treated devices compared to controls. b) Binding energies and schematics of ZnMgO interfaces with metal oxides. c) ZnMgO trap emission spectra for ZnMgO and ZnMgO/Al_2O_3. d) TOF-SIMS profile of elements in ITO/ZnMgO/Al_2O_3. e) Cross-sectional TEM images of LEDs with and without Al_2O_3 treatment. f) Azimuthally integrated intensities of the GISAXS diffraction peak for ZnMgO (green) and ZnMgO/Al_2O_3 (blue) film samples. The ZnMgO/Al_2O_3 films (blue) exhibit a ≈25% increase in d spacings, and peaks narrower by ≈40% compared with ZnMgO films (green).

voltage (I-V) characteristics before and after aging and used space-charge limited current (SCLC) analysis to obtain the trap state density[26,27] (see calculation in supplementary information note 3). SCLC analysis revealed that aging decreased the electron trap state density sevenfold, from 14.2×10^{17} to 2.1×10^{17} cm^{-3} (Figure 2b). This significant reduction in trap states explains the decrease in the dark current (Figures 1b and 2b), since fewer defect-assisted recombination pathways are available for thermally excited carriers.[28,29]

To gain a deeper understanding of how the reduction in trap density of ZnMgO NCs impacts the photo-physics of the InP QD emissive layer, we examined the time-resolved PL of InP QDs in devices before and after aging. The aged device showed a 37% longer lifetime compared to its fresh counterpart (Figure 1f; Figure S3, calculations in Supporting Information). In parallel, we monitored the PL of the poly-TPD/InP QD sample before and after aging and observed a decrease in both PL intensity and lifetime (Figure S4, Supporting Information). Conversely, the PL of the InP QD/ZnMgO sample before and after aging showed an increase in both PL intensity and lifetime (Figure S5, Supporting Information). The improvements in both PL intensity and PL lifetime in the latter case suggest enhanced interfacial passivation of ZnMgO after aging. We propose that improved passivation of the ETL reduced electron trapping, and increased conductivity, as seen in ITO/ZnMgO/Ag devices following positive aging (Figure S6, Supporting Information).

Combining the structural, electrical, and optical characterization data of fresh and aged devices, we propose the following mechanism for positive aging. Initially, the ZnMgO NCs

are size-heterogeneous and possess a high density of surface traps (Figure 2c). Upon aging, the ZnMgO NCs undergo a size-focusing ripening process with neighboring dots, a phenomenon previously observed in ZnO NC synthesis,[30,31] where metal ions from far smaller NCs diffuse and nucleate on larger NCs at reactive sites.[32] A redshift in the absorption spectrum after two weeks is in agreement with this picture of NC size growth. (Figure S7, Supporting Information) This process results in a more size-uniform and closely packed layer with fewer surface traps. Size-uniform ZnMgO results in a more homogeneous energy landscape and the reduced surface traps minimize electron trapping, facilitating electron transport. These factors enhance the conductivity of the ZnMgO layer, and the luminance of the InP QD emissive layer (Figure 2d)[33]. This in turn significantly improves the performance of the devices upon aging.

Though a positive aging process improves device performance over time, achieving consistently high performance across different batches remains a significant challenge. To quantitatively assess this variability, we fabricated ≈30 batches of devices and analyzed their efficiency enhancement upon aging. The EQE data revealed considerable variations (91% ± 66%) in efficiency enhancement, indicating a lack of reproducibility crucial for reliable device performance and industrialization into display technologies (**Figure 3a**).

Improved size uniformity of ZnMgO NCs has the potential to limit the extent of size-focusing ripening. Here we explored instead an approach intended to prevent the ripening process altogether: metal oxide passivation that would, we posited, block the chemical interactions leading to ripening.[20,34,35]
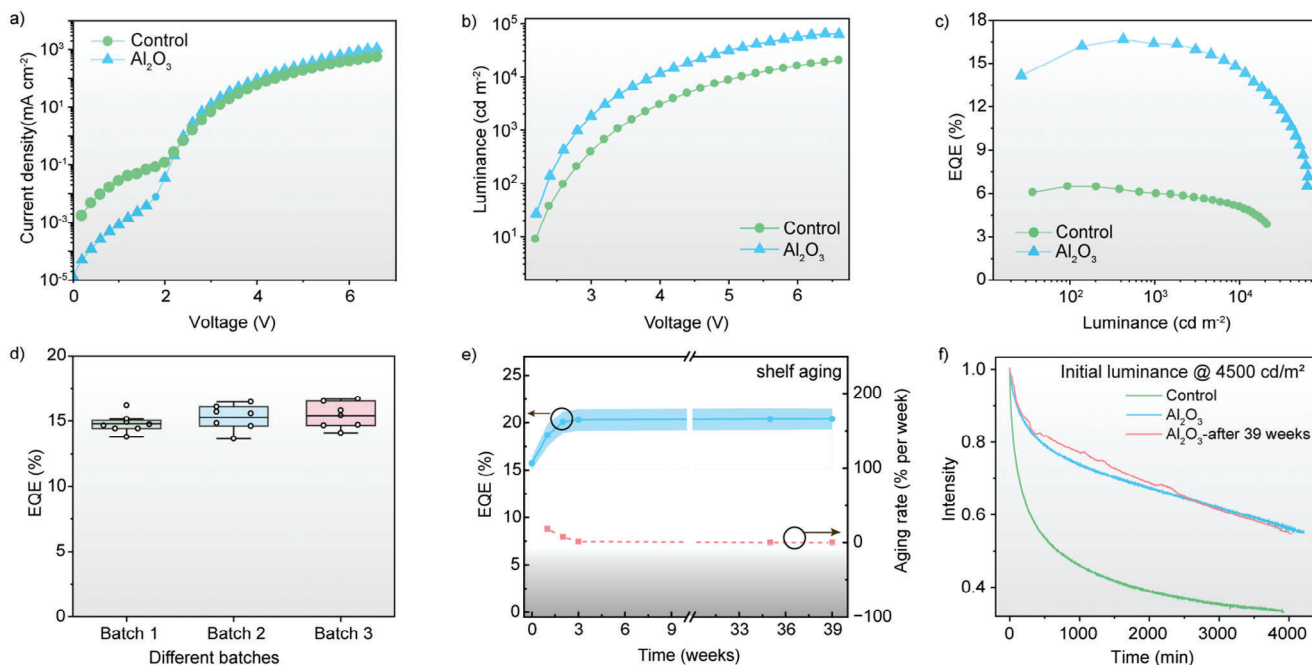
ADVANCED
SCIENCE NEWS
www.advancedsciencenews.com

ADVANCED
MATERIALS
www.advmat.de

Figure 4. Performance of QD-LEDs with and without Al_2O_3. a) Current density-voltage characteristics, b) luminance-voltage characteristics, and c) EQE-luminance characteristics of devices measured immediately after fabrication with and without Al_2O_3. d) Batch-to-batch reproducibility of fresh devices with the Al_2O_3. e) EQE and positive aging rate of devices with Al_2O_3 recorded at different aging periods, with the shaded area representing the error bars. f) Relative luminance vs operation time for freshly fabricated devices with and without the Al_2O_3 and 39-week aged devices with Al_2O_3 under ambient conditions (devices were driven at a constant current density to achieve an initial luminance of 4500 cd m^{-2}).

We began with density functional theory (DFT) studies: the binding (with ZnMgO) of candidate metal oxides, including Al_2O_3, SnO_2 (a widely used conductive ETL),[36,37] and HfO_2 (high dielectric passivation materials).[38–40] Among these, Al_2O_3 is predicted to have the most favorable binding with ZnMgO (Figure 3b). Similarly, Al_2O_3 is reported to have lower trap densities,[41–43] thus an ideal candidate for effective passivation. Furthermore, the charge density difference in ZnMgO/Al_2O_3 sample also shows clear charge transfer between ZnMgO and Al_2O_3, indicating the formation of chemical bonds (Figure S8, Supporting Information).

To study this passivant experimentally, we deposited Al_2O_3 on ZnMgO using ALD. Trap PL of ZnMgO at 505 nm[44,45] after deposition of Al_2O_3 decreased: its associated PLQY decreased from 8% to 5% (Figure 3c). We then compared the PL of InP QDs in a full device stack with and without Al_2O_3 (poly-TPD/InP QD/ZnMgO and poly-TPD/InP QD/ZnMgO/Al_2O_3) samples. Samples with Al_2O_3 showed a 15% increase in PL intensity compared to samples without Al_2O_3 and an increased lifetime from 9.7 to 13 ns (Figure S9, calculations in Supporting Information). These results imply that the Al_2O_3 passivation effectively reduces traps in the ZnMgO layer, which are responsible for the non-radiative recombination of InP QDs.

Metal oxide deposition using ALD results in the atomic-level incorporation of material into structured substrates rather than creating a planarized layer,[35,46–48] which in the current case could lead to full passivation of the ZnMgO NCs. To assess the extent of Al_2O_3 infiltration in the ZnMgO layer, we employed time-of-flight secondary ion mass spectrometry (TOF-SIMS) on a sample structured as ITO/ZnMgO/Al_2O_3 (Figure 3d). TOF-SIMS anal-

ysis revealed significant infiltration of Al_2O_3 into the ZnMgO layer, filling in the gaps between ZnMgO NCs and passivating the ZnMgO surface. To further confirm this, we conducted cross-sectional transmission electron microscopy (TEM) along with energy dispersive spectroscopy (EDS) analysis for our devices with and without Al_2O_3 (Figure 3e). The EDS measurement showed a noticeable increase in Al within the ZnMgO layer, confirming the diffusion of ALD-deposited Al_2O_3 into the ZnMgO layer (Figure S10, Supporting Information). The thickness of ZnMgO increased by $\approx$3 nm, without a distinct overcoating layer on top of the ZnMgO layer, implying that Al_2O_3 has penetrated and expanded the ZnMgO layer thickness.

Next, we used GISAXS to analyze the ZnMgO film with and without Al_2O_3 to see how it affects the physical properties of the NCs. This analysis revealed a $\approx$40% reduction in size distribution and an increase in average size from 4.0 to 5.0 nm after Al_2O_3 deposition (Figure 3f). This suggests an average Al_2O_3 thickness of 0.5 nm, approximately half a monolayer, deposited on each ZnMgO NC. The size distribution reduction we attribute to preferential growth on smaller NCs during ALD, since their higher surface energy and reactivity are expected to favor precursor adsorption, accelerating their growth.[5,49,50] We note that a set of experiments with various ALD conditions on QD-LEDs confirmed that the passivation effect is due to the growth of Al_2O_3 and, not caused by the individual ALD precursors (Figure S11, Supporting Information).

We then examined how the Al_2O_3-passivated ZnMgO layer influences the electrical properties of the LED, in particular the leakage current and forward current over the threshold voltage. Devices with different Al_2O_3 thicknesses showed that leakage

current reduced with increasing thickness. The forward current over the threshold voltage was initially stable but then fell exponentially as Al_2O_3 thickness increased (Figure S12, Supporting Information). This suggests that the first 3 nm of Al_2O_3 deposition passivates ZnMgO NCs, reducing leakage current without affecting forward current. However, subsequent deposition slows electron transport, ultimately blocking both leakage and forward currents.

Motivated by the improved physical properties of ALD-deposited ZnMgO, we implemented these advancements in QD-LEDs. Our device architecture consists of ITO/NiOx/4-CF$_3$-BA/poly-TPD/InP QD/ZnMgO/Al_2O_3/Al, with an optimized Al_2O_3 thickness of 3 nm. (Figure S13, Supporting Information) Both LED types (with and without Al_2O_3) exhibit bright, pure-red emission (EL peak of 635 nm with a full width at half maximum of 38 nm, Figure S14, Supporting Information). Notably, fresh QD-LEDs with ZnMgO passivated by Al_2O_3 show improved current density, enhanced maximum luminance (**Figure 4a,b**), and a higher EQE of 17%, compared to 6.5% achieved by fresh devices without Al_2O_3 (Figure 4c; Figure S15, Supporting Information).

To assess batch-to-batch reproducibility, we fabricated three different batches of fresh QD-LEDs integrated with Al_2O_3. Analysis of 22 devices revealed nearly identical efficiencies, indicating high reproducibility (Figure 4d). We then measured the operational stability of freshly prepared control and Al_2O_3-passivated LEDs under the same condition. QD-LEDs with Al_2O_3 demonstrate a significantly extended operating lifetime (T_{60}) of 60 h at an initial brightness of 4500 cd m^{-2}, compared to only 6 h for devices without Al_2O_3 (Figure 4f).

To understand the long-term aging behavior, we tracked the performance of our devices when stored in an inert environment. A small initial increase in EQE stabilizes after three weeks, resulting in a 30% ± 15% enhancement in efficiency, which remains unchanged for >39 weeks (Figures 3a and 4e). Contrary to this, control devices (without Al_2O_3) EQE falls below the performance of fresh devices over a similar time span. (Figure 1e) After 39 weeks, devices with Al_2O_3-coated ZnMgO show significantly better operational stability than control devices. (Figure 4f; Figure S16, Supporting Information). Moreover, the stability decay mechanism remains unchanged after 39 weeks of storage.

In summary, this study unveils the intrinsic origin of uncontrollable aging in QD-LEDs: primally increased conductivity and surface trap passivation in the ZnMgO ETL layer facilitated by size-focusing ripening of ZnMgO NCs followed by rapid degradation. We addressed this limitation by passivating ZnMgO with Al_2O_3, achieving reproducibly high efficiencies (≈17%) in freshly fabricated devices, a tenfold improvement in T_{60} (60 h at 4500 cd m^{-2}), and substantial improvement in batch-to-batch reproducibility. The Al_2O_3-based devices exhibited excellent stability under shelf-life and continuous illumination conditions. This fundamental progress highlights the critical role of stabilizing NC-based layer stability in achieving durable and reliable LEDs and could serve as a universal strategy for stabilizing NC-based films in various optoelectronic and electrocatalytic applications.

3. Experimental Section

Materials: Oleylamine (OAm, technical grade 70%, Sigma–Aldrich), Oleic acid (OA, technical grade 90%, Sigma–Aldrich), 1-Octadecene (ODE, technical grade 90%, Sigma–Aldrich), Toluene (ACS reagent, ≥ 99.5%, Sigma–Aldrich), Ethyl acetate (ReagentPlus, 99%, Sigma–Aldrich), 4-CF$_3$-BA (98%, Sigma–Aldrich), NiOx nanoparticles (Avantama, P-21, 0.15 wt.%), poly-TPD (American Dye Sources Inc., ADS254BE), ZnO nanoparticle dispersions (Avantama N-10, 2.5 wt.%, 2-propanol) were used directly as received.

InP/ZnSe/ZnS Quantum Dot Synthesis: The red-emitting InP/ZnSe/ZnS QDs were prepared according to a previously reported method.[8] For the synthesis of the InP core, 4 mmol of indium palmitate was prepared in 100 mL of 1-octadecene by degassing at 120 °C for 1 h. Then, the solution was heated to 280 °C under N$_2$ condition, and 2 mmol of 0.2 M tris(trimethylsilyl)phosphine/trioctylphosphine (TOP) was quickly injected into the solution. The reaction temperature was kept at 260 °C. For further growth of the InP cores, 10.5 mmol of 0.2 M indium palmitate and 5.26 mmol of 0.2 M tris(trimethylsilyl)phosphine were added into the flask for 35 min at 260 °C. The InP core was purified and dispersed in toluene for shell growth. 1.6 mmol of zinc oleate was prepared in 80 mL of trioctylamine by degassing at 120 °C for 1 h. Then, the solution was heated to 180 °C under N$_2$ flow, and 0.25 g of InP core and 0.2 mL of HF solution (10 wt.%) were added into the solution. The reaction temperature was kept at 340 °C. 17.6 mmol of 0.4 M zinc oleate and 16 mmol of 0.4 M Se/TOP were added into the solution for ZnSe shell growth. Then, 4.8 mmol of 0.4 M zinc oleate and 6.4 mmol of 1 M S/TOP were added for ZnS shell growth. The QDs were purified with ethanol and dispersed in octane for LED fabrication.

ALD Al_2O_3 Deposition: Al_2O_3 was deposited through the alternate pulsing of trimethylaluminum (TMA) and water over 30 cycles in the PI-COSUN R-200 Advanced ALD system. The chamber maintains a constant temperature of 100 °C throughout the process. The TMA pulsing was conducted with a 150 sccm carrier gas, utilizing a 0.1s pulse time and a 4 s purge time. For the water pulsing, a 200 sccm carrier gas was employed, with a 0.1s pulse time, and a purge time of 6 s.

Device Fabrication: The pre-patterned ITO glasses were sequentially sonicated in deionized water, acetone, and 2-propanol each for 5 min. After drying with nitrogen, the substrates were exposed to UV-ozone treatment for 15 min to remove organic contaminants. 150 µL of diluted NiOx nanoparticle dispersions (Avantama, P-21, 1.5 wt.%) was filtered through a 0.22 µm polytetrafluoroethylene (PTFE) membrane before use and spun-cast at 3000 rpm for 30 s and annealed at 100 °C for 10 min. Annealed NiOx films were UV-ozone treated for 3 min. NiOx substrates were soaked with SAM solutions (2.5 mg mL^{-1} in anhydrous ethanol) for 30 s, spin-cast at 5000 rpm for 20 s, and then annealed at 100 °C for 5 min. Unbound SAM molecules were washed off with pure anhydrous ethanol spin coating at 5000 rpm for 20 s and annealed at 100 °C for 5 min. All HIL-coated substrates were transferred in the N2-filled glovebox, and then 150 µL of poly-TPD in chlorobenzene (6 mg mL^{-1}) solution was filtered through a 0.22 µm PTFE membrane before use and spun-cast at 3000 rpm for 30 s. The films were annealed at 140 °C for 10 min. InP QD solution was filtered through a 0.22 µm PTFE membrane before use and spun-cast at 3000 rpm for 30 s, followed by annealing at 140 °C for 10 min. ZnMgO NCs were prepared according to the literature[51] and the solutions (20 mg mL^{-1} in anhydrous ethanol) were filtered through a 0.22 µm PTFE membrane before use and spun-cast at 3000 rpm for 30 s followed by annealing at 140 °C for 10 min. For the devices with the Al_2O_3 layer, the Al_2O_3 layer (3 nm) was deposited with ALD using the above method. Finally, the films were then transferred to the thermal evaporator (Angstrom engineering), and a patterned Al electrode (100 nm thick) was deposited on top of ZnMgO with a rate of 1.0 Å s^{-1} under a vacuum pressure <2 × 10^{-6} Torr.

LED Performance and Stability Measurement: The J−V characteristics of LEDs were recorded using a Keithley 647 source meter. Electroluminescence spectra and luminance at a certain J−V point were measured using a calibrated fiber-coupled spectrometer (QE-pro, Ocean Optics) and an integrating sphere. To ensure accurate measurements, the calibration of the equipment was performed using a radiometrically calibrated light source (HL-3P-INT-CAL, Ocean Optics). During the measurements, the QD-LED devices were positioned on top of the integration sphere to collect only the forward light emission, following the standard OLED characterization method.[52]

**ADVANCED
SCIENCE NEWS**

www.advancedsciencenews.com

**ADVANCED
MATERIALS**

www.advmat.de

Electron-Only Device Fabrication and Measurement: Electron-only devices with the structure of Glass/ITO/ZnO/InP QD/ZnMgO/Al were fabricated. InP QD, ZnMgO, and Al were fabricated under the same conditions for device fabrication. ZnO nanoparticle dispersion was filtered through a 0.22 μm PTFE membrane before use, spin-coated at 3000 rpm for 30 s, and annealed at 140 °C for 10 min. The J−V characteristics of the electron-only device were measured with a Keithley 2400 source measuring unit.

Cross-sectional Transmission Electron Microscopy: To prepare the cross-sectional LED lamella, fabricated LED samples were first tailored into a dimension of quarter inch by quarter inch. A 5nm carbon coating was deposited on top of the LED surface to disperse charge during following sections. Lamellas were then prepared through Raith VELION FIB-SEM (focused ion beam technology) at MIT.nano. A process of Pt coating, trenching, device top surface under-cutting, manipulator-inserting, manipulator-lamella connecting, lifting, TEM grid driving, lamella attaching, lamella milling, and final thinning/polishing were carried out, consequently. The milled LED lamella was then transferred into the Thermo Fisher Scientific (TFS) Themis Z G3 aberration-corrected scanning transmission electron microscope (STEM) at MIT.nano for imaging.

Synchrotron Grazing Incidence Small Angle Scattering (GISAXS): Synchrotron-based grazing incidence small angle X-ray scattering (GISAXS) data were collected at (SAXS/WAXS) beamline at the Australian Synchrotron.[53] 2D scattering patterns were recorded using an X-ray beam with dimension 150×50 μm^2 [H × V] and an energy of 12 keV (1.0332 Å), and a Pilatus 2 M detector, with the sample-to-detector distance (2.5 m) calibrated using a silver behenate reference standard. The sample and detector were enclosed in a vacuum chamber to suppress air scatter and improve the small angle signal. Scattering patterns were measured as a function of the angle of incidence, with data shown acquired with an angle of incidence near the critical angle to maximize scattering intensity from the target layer in the film ($\approx 0.18°$). The collected 2D images were azimuthally integrated using PyFAI[54] and processed using a custom Python routine.

Photoluminescence Measurements: PL spectra were collected using a Horiba Fluorolog system with a calibrated monochromator and a time-correlated single photon counting detector. For steady-state PL measurements, a xenon lamp was used as the excitation source. For time-resolved PL, a 504 nm laser diode was used with the overall time resolution of $\Delta t = 0.13$ ns limited by the instrument response function.

PLQY Measurements: PLQY measurements were done using a Quanta-Phi integrating sphere coupled to the Horiba Fluorolog system with optical fiber bundles. A monochromatic xenon lamp was used as the excitation source. The Fluorolog was set to an excitation wavelength of 350 nm and to a 5 nm bandpass for both the excitation and emission slits. The detector and integrating sphere were corrected for spectral variance using a Newport-calibrated white light source. The PLQY was calibrated using standard materials with known PLQY values and emissions covering the measurement range, including Coumarin 6, Coumarin 153, and Rhodamine 6G.

TOF-SIMS Measurements: TOF-SIMS measurements were conducted on an IONTOF M6 instrument with a primary Bi source of 30 keV and an analysis area of 50×50 μm^2.

Density Functional Theory Calculation: Spin-polarized DFT calculations were conducted using the projector-augmented wave method,[55] as implemented in the Vienna Ab initio Simulation Package (VASP).[56,57] The generalized gradient approximation (GGA) with the Perdew–Burke–Ernzerhof functional (PBE) was used to describe the exchange-correlation interactions.[58,59] The van der Waals interactions were considered using the DFT-D3 method with Becke-Johnson damping.[60,61] A kinetic cutoff energy of 450 eV was applied. All slab models were considered fully relaxed when the residual force on each ion was reduced to below 0.02 eV Å^{-1}, and energy differences converged within 10^{-5} eV per atom. The ZnMgO bulk structure was obtained by substituting one in eight Zn atoms in the $(2 \times 2 \times 1)$ hexagonal wurtzite ZnO lattice, resulting in the composition of Zn_7MgO_8. A non-polar (2×2) (100) surface model was employed with the back surface passivated using pseudo-hydrogen atoms. The interface model was then constructed by depositing a layer of metal oxides (MO_x = Al_4O_6, Sn_4O_8, or Hf_4O_8) onto the top of the ZnMgO(100) surface. A

vacuum layer exceeding 15 Å was included for all slabs to prevent artificial interactions between the slab and its periodic images. The interfacial binding energy (E_b) was calculated as:

$$E_b = 1/A \times \left(E_{MOx/ZnMgO} - E_{MOx} - E_{ZnMgO} \right) \tag{1}$$

where A is the interfacial area.

Supporting Information

Supporting Information is available from the Wiley Online Library or from the author.

Conflict of Interest

The authors declare no conflict of interest.

Data Availability Statement

The data that support the findings of this study are available from the corresponding author upon reasonable request.

[1] Q. Yuan, T. Wang, P. Yu, H. Zhang, H. Zhang, W. Ji, *Org. Electron.* **2021**, *90*, 106086.

[2] H. Moon, C. Lee, W. Lee, J. Kim, H. Chae, *Adv. Mater.* **2019**, *31*, 1804294.

[3] E. Jang, H. Jang, *Chem. Rev.* **2023**, *123*, 4663.

[4] Y. Shirasaki, G. J. Supran, M. G. Bawendi, V. Bulović, *Nat. Photonics* **2013**, *7*, 13.

[5] A. Alexandrov, M. Zvaigzne, D. Lypenko, I. Nabiev, P. Samokhvalov, *Sci. Rep.* **2020**, *10*, 7496.

[6] S. Mokarian Zanjani, F. Tintori, S. Sadeghi, P. Linkov, S. Dayneko, A. Shahalizad, H. Pahlevaninezhad, M. Pahlevani, *Adv. Photonics Res.* **2022**, *3*, 2200159.

[7] T. Kim, K. H. Kim, S. Kim, S. M. Choi, H. Jang, H. K. Seo, H. Lee, D. Y. Chung, E. Jang, *Nature* **2020**, *586*, 385.

[8] Y. H. Won, O. Cho, T. Kim, D. Y. Chung, T. Kim, H. Chung, H. Jang, J. Lee, D. Kim, E. Jang, *Nature* **2019**, *575*, 634.

[9] H. Y. Xu, J. J. Song, P. H. Zhou, Y. Song, J. Xu, H. B. Shen, S. C. Fang, Y. Gao, Z. J. Zuo, J. M. Pina, O. Voznyy, C. M. Yang, Y. F. Hu, J. Li, J. F. Du, E. H. Sargent, F. J. Fan, *Nat. Photonics* **2024**, *18*, 186.

[10] H. Wan, E. D. Jung, T. Zhu, S. M. Park, J. M. Pina, P. Xia, K. Bertens, Y. K. Wang, O. Atan, H. Chen, Y. Hou, S. Lee, Y. H. Won, K. H. Kim, S. Hoogland, E. H. Sargent, *Small* **2024**, *20*, 2402371.

[11] Q. Su, Y. Sun, H. Zhang, S. Chen, *Adv. Sci.* **2018**, *5*, 1800549.

[12] Z. Chen, Q. Su, Z. Qin, S. Chen, *Nano Res.* **2021**, *14*, 320.

[13] W.-C. Ding, C.-H. Chen, L.-J. Huang, M.-C. Kuo, Y.-P. Kuo, P.-Y. Chen, H.-H. Lu, Y.-H. Lin, N. Tierce, C. J. Bardeen, J.-H. Lee, *SID Symposium Digest of Technical Papers* **2018**, *49*, 1622.

[14] K. P. Acharya, A. Titov, J. Hyvonen, C. Wang, J. Tokarz, P. H. Holloway, *Nanoscale* **2017**, *9*, 14451.

[15] Y.-K. Wang, H. Wan, J. Xu, Y. Zhong, E. D. Jung, S. M. Park, S. Teale, M. Imran, Y.-J. Yu, P. Xia, Y.-H. Won, K.-H. Kim, Z.-H. Lu, L.-S. Liao, S. Hoogland, E. H. Sargent, *J. Am. Chem. Soc.* **2023**, *145*, 6428.

[16] S. Lee, S. M. Park, E. D. Jung, T. Zhu, J. M. Pina, H. Anwar, F.-Y. Wu, G.-L. Chen, Y. Dong, T. Cui, M. Wei, K. Bertens, Y.-K. Wang, B. Chen, T. Filleter, S.-F. Hung, Y.-H. Won, K. H. Kim, S. Hoogland, E. H. Sargent, *J. Am. Chem. Soc.* **2022**, *144*, 20923.

[17] S. Ding, Z. Wu, X. Qu, H. Tang, K. Wang, B. Xu, X. W. Sun, *Appl. Phys. Lett.* **2020**, *117*, 093501.

[18] S. Chen, W. Cao, T. Liu, S.-W. Tsang, Y. Yang, X. Yan, L. Qian, *Nat. Commun.* **2019**, *10*, 765.

[19] X. Duan, J. Ma, W. Zhang, P. Liu, H. Liu, J. Hao, K. Wang, L. Samuelson, X. W. Sun, *ACS Appl. Mater. Interfaces* **2023**, *15*, 1619.

[20] E. G. Dyrvik, J. H. Warby, M. M. Mccarthy, A. J. Ramadan, K.-A. Zaininger, A. E. Lauritzen, S. Mahesh, R. A. Taylor, H. J. Snaith, *ACS Nano* **2023**, *17*, 3289.

[21] Z. Zhang, Y. Ye, C. Pu, Y. Deng, X. Dai, X. Chen, D. Chen, X. Zheng, Y. Gao, W. Fang, X. Peng, Y. Jin, *Adv. Mater.* **2018**, *30*, 1801387.

[22] J. Xu, O. Voznyy, M. Liu, A. R. Kirmani, G. Walters, R. Munir, M. Abdelsamie, A. H. Proppe, A. Sarkar, F. P. Garcia de Arquer, M. Wei, B. Sun, M. Liu, O. Ouellette, R. Quintero-Bermudez, J. Li, J. Fan, L. Quan, P. Todorovic, H. Tan, S. Hoogland, S. O. Kelley, M. Stefik, A. Amassian, E. H. Sargent, *Nat. Nanotechnol.* **2018**, *13*, 456.

[23] K. A. Miller, R. D. Yang, M. J. Hale, J. Park, B. Fruhberger, C. N. Colesniuc, I. K. Schuller, A. C. Kummel, W. C. Trogler, *J. Phys. Chem. B* **2006**, *110*, 361.

[24] H. Zhang, S. Chen, *J. Mater. Chem. C* **2019**, *7*, 2291.

[25] L. Zhang, L. Yin, C. Wang, N. lun, Y. Qi, D. Xiang, *J. Phys. Chem. C* **2010**, *114*, 9651.

[26] L. Xu, J. Li, B. Cai, J. Song, F. Zhang, T. Fang, H. Zeng, *Nat. Commun.* **2020**, *11*.

[27] D.-Y. Son, S.-G. Kim, J.-Y. Seo, S.-H. Lee, H. Shin, D. Lee, N.-G. Park, *J. Am. Chem. Soc.* **2018**, *140*, 1358.

[28] S. Lu, P. Liu, J. Yang, S. Liu, Y. Yang, L. Chen, J. Liu, Y. Liu, B. Wang, X. Lan, J. Zhang, L. Gao, J. Tang, *ACS Appl. Mater. Interfaces* **2023**, *15*, 12061.

[29] B. L. Williams, S. Smit, B. J. Kniknie, K. J. Bakker, W. Keuning, W. M. M. Kessels, R. E. I. Schropp, W. Creatore, *Prog. Photovoltaics* **2015**, *23*, 1516.

[30] E. M. Wong, J. E. Bonevich, P. C. Searson, *J. Phys. Chem. B* **1998**, *102*, 7770.

[31] E. A. Meulenkamp, *J. Phys. Chem. B* **1998**, *102*, 5566.

[32] P. Xia, T. Zhu, M. Imran, J. M. Pina, O. Atan, A. M. Najarian, H. Chen, Y. Zhang, E. Jung, M. Biondi, M. Vafaie, C. Li, L. Grater, A. Khatri, A. Singh, S. Hoogland, E. H. Sargent, *Adv. Mater.* **2024**, 36.

[33] D. Chen, D. Chen, X. Dai, Z. Zhang, J. Lin, Y. Deng, Y. Hao, C. Zhang, H. Zhu, F. Gao, Y. Jin, *Adv. Mater.* **2020**, *32*, 2006178.

[34] E. M. Likovich, R. Jaramillo, K. J. Russell, S. Ramanathan, V. Narayanamurti, *Adv. Mater.* **2011**, *23*, 4521.

[35] Y.-S. Kim, H.-J. Oh, S. Shin, N. Oh, J.-S. Park, *Sci. Rep.* **2022**, 12.

[36] M. M. Tavakoli, H. T. Dastjerdi, P. Yadav, D. Prochowicz, H. Y. Si, R. Tavakoli, *Adv. Funct. Mater.* **2021**, *31*, 2010623.

[37] H. Zhu, S. Teale, M. N. Lintangpradipto, S. Mahesh, B. Chen, M. D. Mcgehee, E. H. Sargent, O. M. Bakr, *Nat. Rev. Mater.* **2023**, *8*, 569.

[38] X. Cheng, P. Repo, H. Halvard, A. P. Perros, E. S. Marstein, H. Di Sabatino, H. Savin, *IEEE J. Photovoltaics* **2017**, *7*, 479.

[39] J. Ephraim, D. Lanigan, C. Staller, D. J. Milliron, E. Thimsen, *Chem. Mater.* **2016**, *28*, 5549.

[40] A. Kala, V. G. Achanta, *The European Physical Journal Special Topics* **2022**, *231*, 799.

[41] K. Y. Chen, C. C. Yang, C. Y. Huang, Y. K. Su, *RSC Adv.* **2020**, *10*, 9902.

[42] Y. Zhang, W. Liu, J. Sun, W. Shou, G. Yu, Q. Yang, W. Yang, B. Yan, J. Sheng, J. Ye, *Physica Status Solidi A Applications and Material Science* **2021**, *218*, 2100406.

[43] L.-F. Wu, Y.-M. Zhang, H.-L. Lv, Y.-M. Zhang, *Chin. Phys. B* **2016**, *25*, 108101.

[44] D. H. Parmar, J. M. Pina, T. Zhu, M. Vafaie, O. Atan, M. Biondi, A. M. Najjariyan, S. Hoogland, E. H. Sargent, *Adv. Mater.* **2022**, *34*, 2200321.

[45] K. Kodama, T. Uchino, *J. Phys. Chem. C* **2014**, *118*, 23977.

[46] R. R. Petit, J. Li, B. Van de Voorde, S. Van Vlierberghe, P. F. Smet, C. Detavernier, *ACS Appl. Mater. Interfaces* **2021**, *13*, 46151.

[47] R. Z. Waldman, D. J. Mandia, A. Yanguas-Gil, A. B. F. Martinson, J. W. Elam, S. B. Darling, *J. Chem. Phys.* **2019**, *151*, 190901.

[48] K. Artuk, D. Turkay, M. D. Mensi, J. A. Steele, D. A. Jacobs, M. Othman, X. Yu Chin, S. J. Moon, A. N. Tiwari, A. Hessler-Wyser, Q. Jeangros, C. Ballif, C. M. Wolff, *Adv. Mater.* **2024**, *36*, 2311745.

[49] Z. Y. Zhou, N. Tian, J. T. Li, I. Broadwell, S. G. Sun, *Chem. Soc. Rev.* **2011**, *40*, 4167.

[50] H. Z. Zhang, R. L. Penn, R. J. Hamers, J. F. Banfield, *J. Phys. Chem. B* **1999**, *103*, 4656.

[51] L. Qian, Y. Zheng, J. Xue, P. H. Holloway, *Nat. Photonics* **2011**, *5*, 543.

[52] S.-H. Jeong, J. Park, T.-H. Han, F. Zhang, K. Zhu, J. S. Kim, M.-H. Park, M. O. Reese, S. Yoo, T.-W. Lee, *Joule* **2020**, *4*, 1206.

[53] N. M. Kirby, S. T. Mudie, A. M. Hawley, D. J. Cookson, H. D. Mertens, N. Cowieson, V. Samardzic-Boban, *J. Appl. Crystallogr.* **2013**, *46*, 1670.

[54] G. Ashiotis, A. Deschildre, Z. Nawaz, J. P. Wright, D. Karkoulis, F. E. Picca, J. Kieffer, *J. Appl. Crystallogr.* **2015**, *48*, 510.

[55] P. E. Blochl, *Phys Rev B Condens Matter* **1994**, *50*, 17953.

[56] G. Kresse, D. Joubert, *Phys Rev B Condens Matter* **1999**, *59*, 1758.

[57] G. Kresse, J. Furthmuller, *Phys Rev B Condens Matter* **1996**, *54*, 11169.

[58] J. P. Perdew, K. Burke, M. Ernzerhof, *Phys. Rev. Lett.* **1996**, *77*, 3865.

[59] J. P. Perdew, J. A. Chevary, S. H. Vosko, K. A. Jackson, M. R. Pederson, D. J. Singh, C. Fiolhais, *Phys Rev B Condens Matter* **1992**, *46*, 6671.

[60] S. Grimme, J. Antony, S. Ehrlich, H. Krieg, *J. Chem. Phys.* **2010**, *132*, 154104.

[61] S. Grimme, S. Ehrlich, L. Goerigk, *J. Comput. Chem.* **2011**, *32*, 1456.